Electrochimica Acta 461 (2023) 142654

Contents lists available at ScienceDirect

Electrochimica Acta

journal homepage: www.journals.elsevier.com/electrochimica-acta

N-functionalization and defect engineering in $ZnCo_2O_4$ nanosheets boosted the performance of Zn-ion hybrid supercapacitor

Xiaofeng Zhang [a], Muhammad Sufyan Javed [a,*], Syed Shoaib Ahmad Shah [b], Fahim Ahmed [c], Iftikhar Hussain [d], Fatimah M. Alzahrani [e], Norah S. Alsaiari [e], Sayed M. Eldin [f], Mohd Zahid Ansari [g,*], Weihua Han [a,*]

[a] School of Physical Science and Technology, Lanzhou University, Lanzhou, 730000, China
[b] Department of Chemistry, School of Natural Sciences, National University of Sciences and Technology, Islamabad, 24090, Pakistan
[c] Department of Physics, Division of Science & Technology, University of Education, Lahore, 54770, Pakistan
[d] Department of Mechanical Engineering, City University of Hong Kong, 83 Tat Chee Avenue, Kowloon, Hong Kong
[e] Department of Chemistry, College of Science, Princess Nourah bint Abdulrahman University, P .O. Box 84428, Riyadh 11671, Saudi Arabia
[f] Faculty of Engineering and Technology, Future University in Egypt, New Cairo, 11835, Egypt
[g] School of Materials Science and Engineering, Yeungnam University, 280 Daehak-Ro, Gyeongsan, Gyeongbuk 38541, Republic of Korea

ARTICLE INFO

Keywords:
Zinc-ion supercapacitors
N-doped
Oxygen vacancy
Pseudocapacitive
$ZnCo_2O_4$

ABSTRACT

Transition-metal oxides are a class of promising pseudocapacitive materials for high energy density supercapacitors, while their low intrinsic conductivity and remarkable volume expansion deteriorate the electrochemical properties. Herein, we develop a binder-free mesoporous architecture supported on a carbon cloth (CC) substrate based on the nitrogen (N)-doped and oxygen vacancy (Ov)-rich zinc cobalt oxide nanosheets (denoted by N-Ov-ZCO@CC). Because of the instructive synergy of doping, defect, and surface engineering achieved by N-functionalization, the N-Ov-ZCO@CC exhibits significantly enhanced electrochemical properties. The N-Ov-ZCO@CC single electrode exhibited a high capacitance of 2166.4 F/g at 1 A/g with superb rate-capability (91.2% at 20 A/g) and superior cycling stability of 98.99% up to 5,000 cycles. In addition, a zinc-ion hybrid supercapacitor (ZHSC) device, assembled with the N-Ov-ZCO@CC as the cathode and Zn-foil as the anode, shows a high energy density of 95.35 Wh/kg at the power density of 10,008 W/kg, superior to most state-of-the-art ZHSCs. This work provides an effective strategy for constructing multifunctional electrochemical energy materials for ZHSCs.

1. Introduction

With the rapid development of the modern electronic industry and the increasingly severe issue of environmental pollution, the demands for high-performance, efficient, and environmental-friendly energy storage devices have greatly increased [1]. Supercapacitors (SCs) are emerging as one of the most compelling candidates for their higher power density, good reversibility, long life span, and safe nature, making them a better choice than lithium-ion batteries [2,3] and potassium ion batteries [4]. Due to the abundant zinc resource, safety, and low manufacturing cost, zinc-ion based energy storage devices have received widespread attention [5–7].

However, the slow migration kinetics of Zn ions leads to poor ZHSCs performance. ZHSCs are currently lacking high-performance cathode materials. Many types of cathode materials are presently being investigated, including vanadium-based materials [8–11], manganese-based materials [12–16], and cobalt-based materials [17–20]. Generally, layered transition metal oxides can be potential cathode materials in ZHSCs, showing a reversible cation/extraction mechanism [21]. Among these materials, $ZnCo_2O_4$ (ZCO) nanosheets attract researchers' interest because of their larger specific surface area, multiple valence states (Co^{2+} and Co^{3+}), low toxicity, and rich redox chemistry [22]. Nevertheless, the electrochemical performances of ZCO are mainly restricted by its insufficient material utilization efficiency and poor electronic conductivity. The primary strategy implemented is to alleviate the obstruction of ZCO nanosheets with conductive metal or carbonaceous materials. Although many efforts have been made [23–26], the enhancement in the electrode's intrinsic conductivity and active

* Corresponding authors.
E-mail addresses: safisabri@gmail.com (M.S. Javed), zahid.smr@yu.ac.kr (M.Z. Ansari), hanwh@lzu.edu.cn (W. Han).

https://doi.org/10.1016/j.electacta.2023.142654
Received 29 October 2022; Received in revised form 12 May 2023; Accepted 24 May 2023
Available online 28 May 2023

material utilization ratio is still inadequate, restricting the ZCO/-conductor interface.

If the electrical conductivity of transition metal oxides could be intrinsically improved without the addition of conductive additives, their rate capabilities and electron transport would be substantially enhanced. At the same time, if more active sites (oxygen vacancies) could be exposed to the surface of the transition metal oxide-based electrode, their capacitance values would be effectively improved. So, it is still a big challenge to construct smooth conductivities pathways and controllable oxygen vacancies for various energy technologies [27].

As an efficient solution, N-atoms doping can enhance the intrinsic activity over each site of metallic oxides by optimizing those electronic structures, thus increasing the electronic conductivity [28,29]. The lone-pair electrons around N atoms can better interact with the metal atoms; the resulting Metal-O-N bonds have longer bond lengths and higher electronegative than the pristine Metal-O bonds, which weakness attraction of Co^{2+}/Co^{3+} to the 3d electrons and decreases the electron transport energy, which improves the reactions kinetics [30]. The embedded N atoms in the lattice of metallic oxides will substitute the place of partially innate O atoms, resulting in a significant number of oxygen defects. The existence of defects will disturb the surrounding atoms to some extent and induce lattice distortion in the crystalline materials, which can effectively regulate the electronic structure, chemical properties, and electrical conductivity of the materials [31].

We proposed that the NH_3 gas can simultaneously perform N-doping and nanoscale surface modification with controlled manipulation of oxygen vacancies into ZCO by active N-species. Nitrogen affect the work function as a dopant by introducing impurity states in the bandgap after mixing an additional N-2p state with the O-2p valence band [32]. The synergistic effects of oxygen vacancies and massive multivalent metal cations, the optimized ZCO electrode (as the anode for ZHSC) with enhanced electronic conductivity, extraordinary rate capacity, and impressive capacity. Therefore, the befitting N-doping and oxygen vacancies contribute to eliminating the obstacles to the electrochemical properties of ZCO. Furthermore, it is well known that the specific surface area (SSA) and pore size distribution of the porous active substances significantly affect the electrolyte permeation and ion transport kinetics, thereby affecting the overall electrochemical abilities of the electrode material. The mesoporous (2–50 nm) materials with high SSA and rich 3D pore networks will increase the electrode-electrolyte interface area and alleviate the volume change during the charging and discharging process. So, a practical design, which aims at integrating doping, defects, and surface-structural engineering, is significant to improve the charge storage ability, rate capability, and cycle stability of ZHSC electrode materials, which was barely reported in previous works.

In this work, the novel N-doped and oxygen vacancy-rich nanosheet architecture is constructed on CC with the help of Chemical Vapor Deposition (CVD). The doping and oxygen vacancy for modulating the electronic configuration enhances the availability of active sites of the N-Ov-ZCO@CC, which significantly increases electron mobility and boosts the reaction kinetics. In a three-electrode system, the N-Ov-ZCO@CC possesses a high capacitance of 2166.4 F/g at 1A/g with superb rate-capability (91.2% at 20 A/g). The N-Ov-ZCO@CC as cathode and Zn foil as an anode is used to assemble the ZHSC (N-Ov-ZCO@CC//Zn). The N-Ov-ZCO@CC//Zn-ZHSC shows promising electrochemical performance. These superb electrochemical properties reflect its massive potential in the field of ZHSCs.

2. Experimental section

2.1. Materials

Zinc nitrate hexahydrate ($Zn(NO_3)_2{\cdot}6H_2O$), Cobalt nitrate hexahydrate ($Co(NO_3)_2{\cdot}6H_2O$), Ammonium fluoride (NH_4F), urea (CH_4N_2O), Potassium hydroxide (KOH), Zinc acetate ($Zn(AC)_2$), Carbon Clothes (CC), etc., were purchased from Shanghai Aladdin Chemical Reagent Co. All chemical reagents were used as received without any purification and further-treatment.

2.2. Synthesis of ZCO@CC and N-Ov-ZCO@CC

The carbon clothes supported $ZnCo_2O_4$ nanosheets were prepared using a simple hydrothermal method. First, the CC was pretreated with 18 mol/L H_2SO_4 for 6 h to eliminate the undesirable organic impurities and enhance the surface hydrophilicity. Second, to increase the hydrophilic groups on the surface of CC, the CC was annealed at 600 °C in an air atmosphere for 2 h at the heating rate of 5 °C/min. Third, 6.0 mmol $Co(NO_3)_2{\cdot}6H_2O$ and 3 mmol $Zn(NO_3)_2{\cdot}6H_2O$ were dissolved into 80 mL deionized water and magnetically stirred for 10 min to form a clear red solution. After adding 4 mmol NH_4F and 12 mmol urea, stirred for another 30 min. The solution of 80 mL and the cleaned carbon clothes were transferred into the 100 mL Teflon-lined stainless-steel autoclave and heated to 130 °C for 5 h. After cooling the autoclave to room temperature, the product was rinsed with deionized water and alcohol several times and dried at 60 °C for 12 h to get the precursor of ZCO@CC. To convert the precursor to crystalline ZCO@CC, the sample was annealed at 350 °C in an air atmosphere for 2 h at the heating rate of 5 °C/min. And to get the N-Ov-ZCO@CC, the ZCO@CC was annealed in ammonia gas flow (50 ml/min) at temperatures of 350 °C for 2 h at the heating rate of 5 °C/min. The N-Ov-ZCO@CC and ZCO@CC electrodes were used in 1 cm^2-area, and the electrode materials were loaded with 1.17 mg/cm^2 and 1.09 mg/cm^2, respectively.

2.3. Characterization

An X'pert pro-X-ray diffractometer was used to study the X-ray diffraction (XRD) patterns. Scanning electron microscopy (SEM) measurements were performed with an Apreo S microscope (Thermo Fisher Scientific, US). An ethanol suspension of the sample was placed onto Cu grids, which were used for transmission electron microscopy (TEM) analysis on a Tecnai F30 Transmission Electron Microscope (FEI, Netherlands). Elemental analysis by X-ray photoelectron spectroscopy (XPS) was carried out on a Kratos AXIS Ultra DLD X-ray photoelectron spectrometer (Kratos, UK). Election paramagnetic resonance (EPR) test was carried out in the X-band (9.45 GHz) with 5.00-G modulation amplitude and a magnetic field modulation of 100 kHz by a EPR spectrometer (JES-FA300, JEOL) at 77 K. And the N_2 adsorption/desorption isotherms were tested to study the specific surface area via Brunauer-Emmett-Teller (BET) analysis and the pore volume and pore size distribution via the Barrett-Joyner-Halenda (BJH) analysis (Micromeritics, ASAP2020).

2.4. Electrochemical measurements

The three-electrode system was used to investigate the electrochemical performance of the ZCO@CC and N-Ov-ZCO@CC as a single electrode in 6 M KOH + 0.2 M Zn-acetate aqueous electrolyte. A 1 cm^2-area Pt plate was the auxiliary electrode, and an Ag/AgCl electrode was the reference electrode. The electrochemical activity of the working electrodes was evaluated by cyclic voltammetry (CV), galvanostatic charge-discharge (GCD), and electrochemical impedance spectroscopy (EIS) (1mHz to 1 MHz) using a CS2350 Electrochemical Workstation.

The two-electrode system was used to investigate the electrochemical performance of the N-Ov-ZCO@CC//Zn-ZHSC device in 6 M KOH + 0.2 M Zn-acetate aqueous electrolyte. The N-Ov-ZCO@CC served as the cathode and the Zn foil as the anode in the ZHSCs device. The mass of Zn foil with dimensions of 1 × 1 cm^2 is 425.92 mg/cm^2. The performance parameters of the device were assessed by CV, GCD cycles, EIS, and energy and power densities.

In addition, CV and GCD tests were performed under a three-electrode system using a 1 cm^2-area pristine CC as the working electrode, a 1 cm^2-area Pt plate as the auxiliary electrode, and an Ag/AgCl

electrode as the reference electrode. The mass density of the pristine CC was measured to be 11.82 mg/cm^2, and other properties (such as surface area, thickness, and strength) are provided in Table S1. According to the GCD curves, the specific capacitance at a current density of 1 A/g is calculated to be 355.6 F/g at 1 A/g, so the computed area-specific capacitance is 0.41 F/cm^2. Based on these values, we excluded the contribution of CC from the ZCO@CC and N-Ov-ZCO@CC to avoid overestimating the value of specific capacitance.

2.5. Calculations

To calculate the specific capacitance (C) through the charge/discharge curves, the following equation is applied where C (F/g) is the gravimetric specific capacitance, $\frac{I}{m}$ (A/g) is the specific current density, m (g) is the mass of the active material, ΔV (V) is the potential window, and Δt (s) is the discharge time.

$$C = \frac{I\Delta t}{m\Delta V} \tag{1}$$

In a two-electrode system, the power (P) and energy (E) densities of a ZHSC are essential parameters that can be calculated according to Eqs. (2) and (3) [33,34] based on the mass of active materials and based on the total mass of the device including the mass of substrates. The total mass of the device is 438.87 mg/cm^2.

$$E = \frac{1}{2}C(\Delta V)^2 \times \left(\frac{1000}{3600}\right) \tag{2}$$

$$P = \frac{3600 \times E}{\Delta t} \tag{3}$$

where the unit of specific energy density is Wh/kg and W/kg for power density.

3. Results and discussion

The binder-free fabrication process of ZCO and the formation of N-Ov-ZCO nanosheets on the flexible carbon clothes (CC) substrate is schematically explained in Fig. 1. The uniform construction of ZCO nanosheets was directly grown on the CC substrate by a sample and cost-effective hydrothermal process. The well-crystalline ZCO nanosheets and N-Ov-ZCO nanosheets at CC were obtained after calcinating the precursor at 350 °C in the air and NH_3 atmosphere, respectively.

The morphology and structure of the ZCO@CC and N-Ov-ZCO@CC samples were investigated by SEM. Fig. S1 shows the SEM images of the clean CC sample. The CC was pretreated with 18 mol/L H_2SO_4 for 6 h after it was annealed at 600 °C in an air atmosphere for 2 h at the heating rate of 5 °C/min. It is to eliminate undesirable organic impurities and enhance the hydrophilic groups on the surface of CC. The nanosheets are vertically spread to avoid aggregation like the powder sample, which could make the active substance on the CC surface fully in contact with the electrolyte so that the prepared samples have excellent electrochemical performance [35]. From the enlarged SEM image (Fig. 2c), it can be seen that ZCO nanosheets are composed of many interconnected nanowires. The N-Ov-ZCO nanosheets are uniformly distributed on the CC after sintering in NH_3 (Fig. 2d–f). Compared with ZCO, the morphology is not changed, showing good stability. As demonstrated in Fig. 2e, the cross-sectional top-view image of N-Ov-ZCO@CC has symmetrically covered the CC and shaped it as a hierarchical nanosheet-type structure [36]. Fig. 2f shows that N-Ov-ZCO nanosheets are vertically distributed on the CC, and multiple nanosheets are connected to each other to form many holes, which facilitates the rapid Faraday reaction.

To further analyze the microstructure of the samples, TEM characterization was performed. Fig. 2g-h shows the TEM image of N-Ov-ZCO nanosheets at different magnifications, from which we can notice that nanosheets are made of many particles stacked on top of each other and encapsulated carbon layer, thus presenting many interstices at the nanoscale (Fig. 2h). The formation of such morphologies is associated with the thermal decomposition of the ZCO precursor in the NH_3

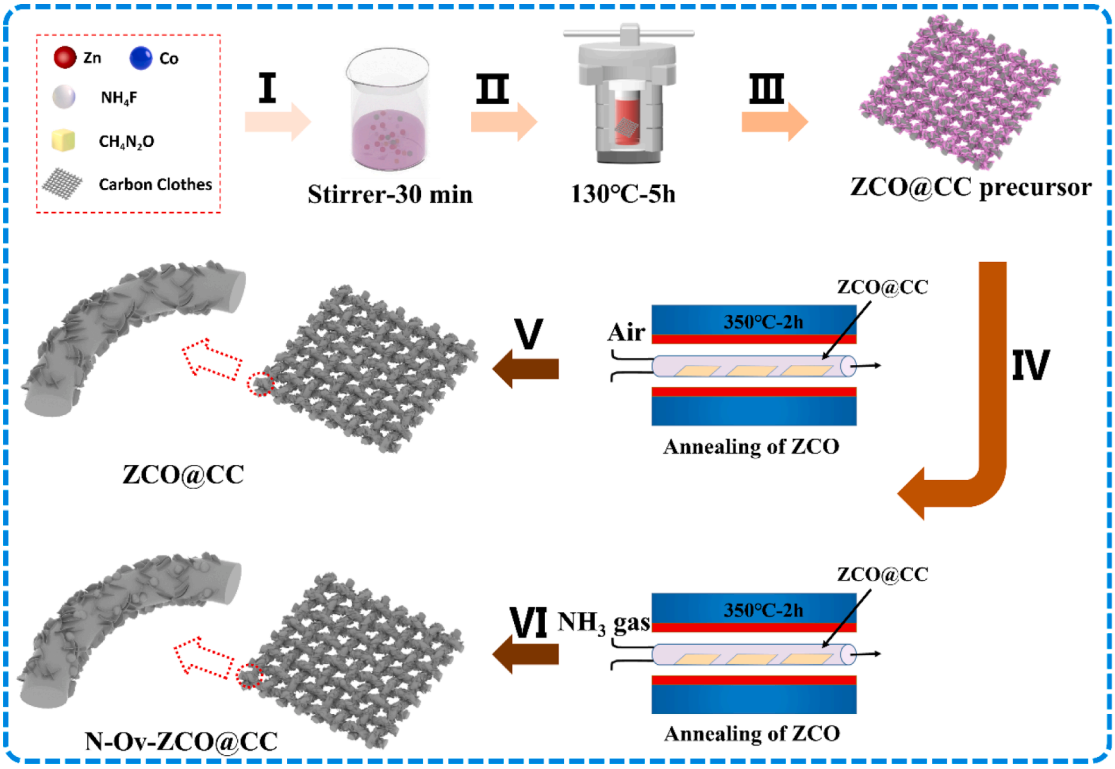

Fig. 1. Schematic diagram for hydrothermal preparation of ZCO@CC and N-Ov-ZCO@CC nanosheets.

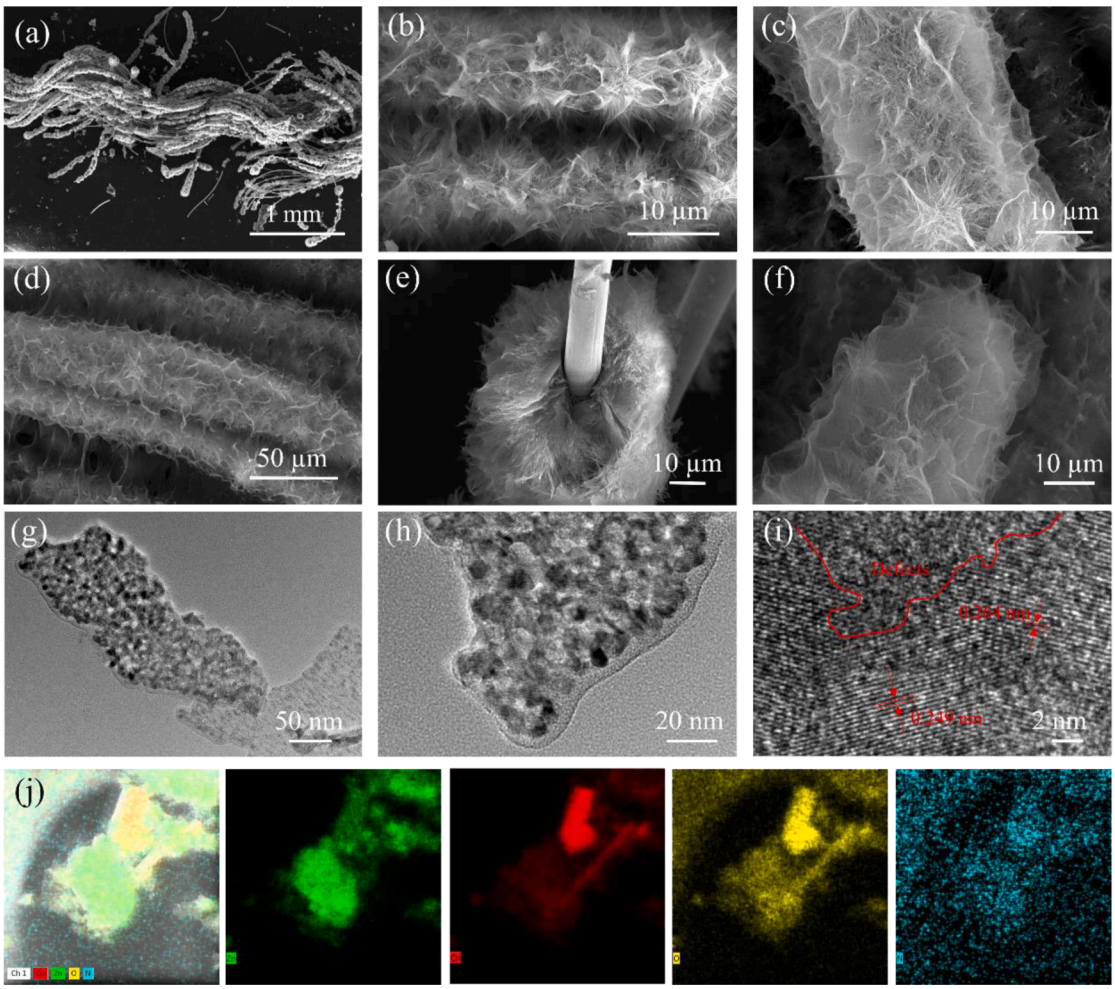

Fig. 2. (a-c) Low and high-magnification SEM images of the ZCO@CC. (d-f) Low and high-magnification SEM images of the N-Ov-ZCO@CC. (g, h) Low and high-magnification TEM images of the N-Ov-ZCO nanosheets. (i) HRTEM images of the N-Ov-ZCO nanosheets, the lattice spacing is 0.264 nm and 0.249 nm. (j) STEM image and elemental mappings of the N-Ov-ZCO@CC.

annealing process, which simultaneously induces and decrease the grain sizes and produce the defects with a carbon layer. Therefore, increasing the specific surface area and such a hierarchical structure can provide more active sites, significantly improving the electrochemical performance. HRTEM images of N-Ov-ZCO (Fig. 2i) show that the lattice spacing of 0.249 nm and 0.264 nm corresponds to the (400) and (331) crystal planes of ZCO, respectively. Furthermore, the elemental mapping confirmed the uniform and homogeneous distribution of N, Zn, Co, and O elements (Fig. 2j).

Fig. 3a compares the XRD patterns of pristine ZCO@CC and N-Ov-ZCO@CC that were explicitly established on CC (after being calcined at 350 °C). The observed XRD patterns could associate with the space category Fd3m (JCPDS no: 23-1390) to a cubic spinel phase ZCO and were confirmed and align with literature [37]. The peaks of diffraction at 19.02°, 31.66°, 37.10°, 59.51°, and 65.48° can be indexed to the planes of (111), (220), (311), (511), and (440), respectively. And an intense diffracting peak located around 26.36 °corresponds with the carbon cloth (300) plane (JCPDS no: 50-0927). ZCO has a typical spinel configuration, with divalent Zn-ions occupying the tetrahedral sites and trivalent Co-ions taking up the octahedral sites. It contains 32 O atoms in the crystallographic unit cell structure [38]. The peak at 42.81 is attributed to the substitution of oxygen vacancies by nitrogen atoms. By comparison, a slight weakening of the N-Ov-ZCO's crystallinity occurs, suggesting that N atoms are doped into the lattice oxygen position of the ZCO without altering the crystal structure [39]. Moreover, the slight reduction of diffraction angle for all the characteristic peaks of the N-Ov-ZCO is ascribed to the N atoms with larger atomic radii prompting the lattice expansion of the ZCO [39].

To further characterize the elemental composition and oxidation state of the ZCO@CC and N-Ov-ZCO@CC, X-ray photoelectron spectrum (XPS) measurement was used, and the results are presented in Fig. 3b-f. The XPS survey spectra indicate the presence of Co, Zn, C, and O in ZCO@CC, and the presence of Co, Zn, N, C, and O in N-Ov-ZCO@CC (Fig. S2). XPS spectrum indicated that nitrogen atoms were successfully incorporated into the ZCO@CC sample. As shown in Fig. 3b, the two peaks with binding energy values at 1020.5 and 1043.7 eV are ascribed to Zn $2P_{3/2}$ and Zn $2P_{1/2}$ spin-orbit peaks of ZCO@CC, respectively. The XPS measurement revealed that the Zn and Co radio is close to 1:2 in the ZCO@CC. And the two peaks with binding energy values at 1021.5 and 1044.5 eV are ascribed to Zn $2P_{3/2}$ and Zn $2P_{1/2}$ spin-orbit peaks of N-Ov-ZCO@CC, respectively. The Zn $2P_{3/2}$ and Zn $2P_{1/2}$ of N-Ov-ZCO@CC are shifted from slightly higher energy levels on the surface may be attributed to the oxygen vacancy generated by nitrogen atoms doping [40,41].

Meanwhile, the core-level Co 2p of ZCO@CC and N-Ov-ZCO@CC is displayed in Fig. 3c. Two pairs of dominant peaks were assigned to the Co $2P_{3/2}$ and Co $2P_{1/2}$ energy level of the Co element, respectively [42]. The characteristic peaks 779.4 (Co $2p_{3/2}$) and 794.5 (Co $2p_{1/2}$) eV of Co^{3+} in ZCO@CC are formed, respectively. And the characteristic peaks 781.5 (Co $2p_{3/2}$) and 796.6 (Co $2p_{1/2}$) eV of Co^{2+} in ZCO@CC are formed, respectively. The characteristic peaks 780.6 (Co $2p_{3/2}$) and 796.7 (Co $2p_{1/2}$) eV of Co^{3+} in N-Ov-ZCO@CC move in the direction of

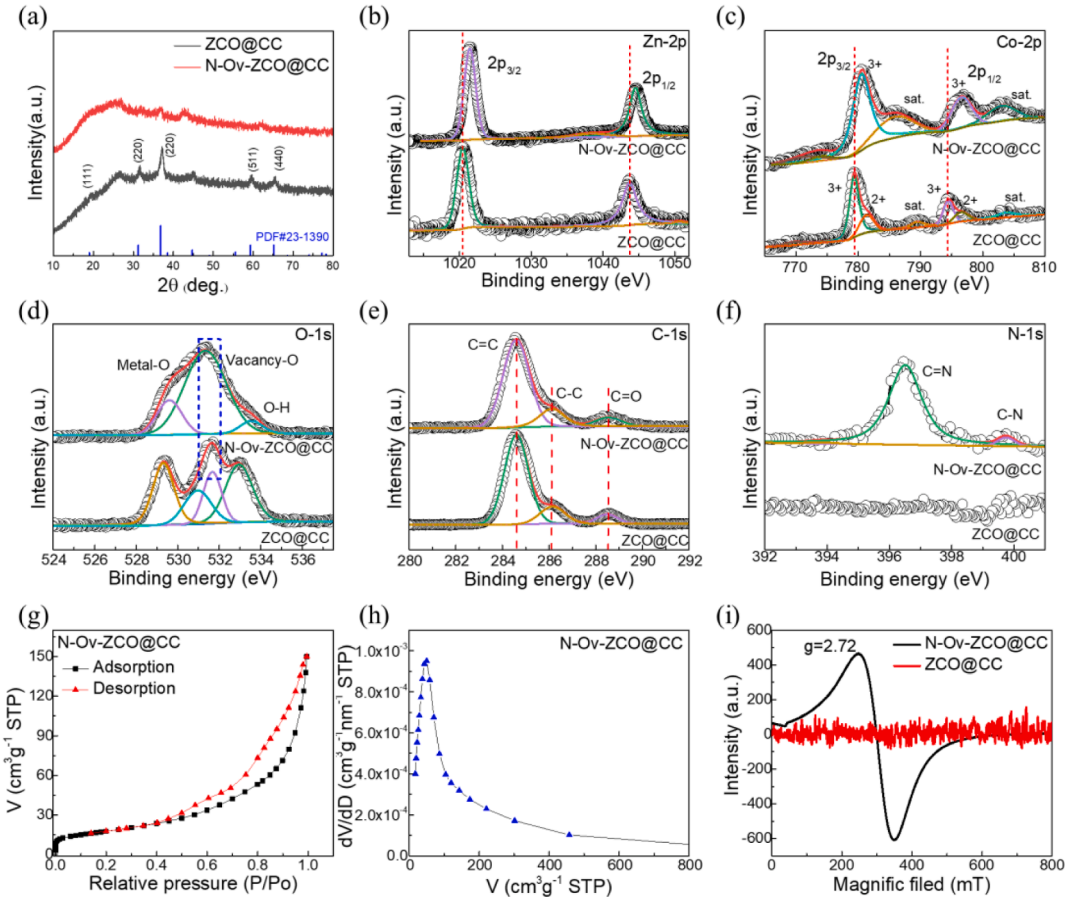

Fig. 3. (a) XRD patterns of the ZCO@CC and N-Ov-ZCO@CC samples. (b-f) Deconvoluted XPS spectra of Zn-2p, Co-2p, O-1s, C-1s and N-1s, respectively. (g-h) N_2 adsorption/desorption isotherms and pore-size distribution curve. (i) EPR spectra of the N-Ov-ZCO and ZCO.

high binding energy, which is important to promoting redox reaction and improving the electrochemical performance of ZHSCs. The characteristic peaks Co $2p_{3/2}$ and Co $2p_{1/2}$ of Co^{2+} in N-Ov-ZCO@CC disappear. Only the presence of Co^{3+} in N-Ov-ZCO@CC indicates that Co^{2+} is oxidized to Co^{3+} by NH_3. Another two pairs of dominant peaks are the corresponding satellite peaks.

Furthermore, the oxygen vacancies in the samples were investigated using the O 1s spectrum. Fig. 3d displays the O 1s spectrum of ZCO@CC and N-Ov-ZCO@CC with three oxygen contributions, which symbolize the metal-oxygen bond (Metal-O), oxygen vacancy (V_o), and hydroxyl groups (H—O—H) on the surface of the samples. The peak of the oxygen vacancy increased in the N-Ov-ZCO@CC compared with ZCO@CC; the addition of N atoms increased the surface oxygen vacancy of the N-Ov-ZCO@CC sample. The absence of oxygen allowed the metal to retain abundant partial charge, facilitating fast charge transport [43]. As shown in Fig. 3e, the C 1s spectrum of the pristine state presents three peaks at 284.6, 286.1, and 288.6 eV, which belong to C═C, C—C, and C═O, respectively. No shift in the central peak of C 1s was observed after the addition of N atoms. N 1s spectrum of the pristine state presents two peaks in N-Ov-ZCO@CC, which belong to C═N and C—N, respectively (Fig. 3f). However, no peaks of N atoms were found in ZCO@CC, which proved that nitrogen atoms were successfully incorporated into ZCO@CC after NH_3 functionalization.

Specific surface area, porosity, and average pore diameter greatly affect the properties of SC's electrode material; it plays a decisive role in electrochemical performance [44]. As shown in Fig. 3g, N_2 adsorption-desorption measurements were investigated for the textural properties of N-Ov-ZCO@CC. Rapid uptake at high relative pressure was identified as the isotherm as a type IV with H_3 hysteresis loop, which is relevant to the mesoporous-like materials [45]. Distinctive hysteresis loop from 0.0 to 1.0 P/P_0 belongs to the typical Langmuir IV isotherms. It confirms the existence of plentiful mesopores, which results in the high BET-specific surface area of N-Ov-ZCO@CC up to 63.47 m^2/g, notably suitable for energy storage applications. The high specific surface area of N-Ov-ZCO@CC originates from their porous structure. Such a structure is favorable to supercapacitors because the porous structure with a large specific surface area can facilitate the electrolyte ion diffusion, enhance the charge transport, and provide more electroactive sites for fast energy storage [46]. The corresponding pore size distribution (Fig. 3h) calculated by the Barrett-Joyner-Halenda (BJH) method from the desorption branch further confirms the characteristic of the mesoporous structure. The pore diameters sharply center at 46.88 nm, which signifies the hierarchical mesoporous features [47]. This porosity is mainly due to multiple centered mesopores, which enhance mass transport of N-Ov-ZCO@CC and improve electrode active surface area utilization. High specific surface area and mesoporous channels facilitate ion/electron transport dynamics, achieving high-rate capabilities and energy/power densities by providing sufficient active sites for the Faraday reaction.

To test the presence of oxygen defects in the N-Ov-ZCO@CC, EPR is performed (Fig. 3i). Compared with the ZCO@CC, considering that oxygen vacancy with the unpaired electron is the main reason for the EPR response in such kinds of materials, the higher intensity of EPR response for N-Ov-ZCO@CC at $g = 2.72$ demonstrate that the continuous plasma activation instigates the formation of abundant oxygen defects.

The pristine CC electrode's CV (Fig. S3) and GCD (Fig. S4) curves were performed to find the potential contribution from the CC substrate. Compared to the N-Ov-ZCO@CC and ZCO@CC electrodes, we found that

the contribution of the pristine CC electrode to capacitances is small (Fig. S5). However, we have excluded the capacitance values of the pristine CC electrode from the N-Ov-ZCO@CC and ZCO@CC electrodes.

Typical CV curves of ZCO@CC and N-Ov-ZCO@CC electrodes at a fixed scan rate of 5 mV/s in a potential range of 0.0–0.5 V are depicted in Fig. 4a. It's not hard to see that N-Ov-ZCO@CC possess higher area under the CV curves than ZCO@CC and the pristine CC electrode (Fig. S3), hence having more charge storage capability. A pair of sharp and symmetrical redox peaks with an anodic peak at 0.18 V and a cathodic peak at 0.27 V is observed for each electrode, which is attributed to the reversible Faradaic redox reactions primarily associated with the transitions of Co^{2+}/ Co^{3+}/ Co^{4+} for ZCO@CC [48].

This distinctive and synergetic redox mechanism promises to afford higher available Faradic pseudo capacitance in the charge/discharge process. For further investigation, we used the N-Ov-ZCO@CC electrode to record CV curves at various scanning rates (1–75 mV/s) in the potential range of 0.0–0.5 V, as shown in Fig. 4b. As the scan rate increases, the CV of N-Ov-ZCO@CC curves shows good preservation of shape, suggesting rapid mass transport at the electrode/electrolyte interface. The CV curves at various scanning rates (1–75 mV/s) in the potential range of 0.0–0.5 V of ZCO@CC electrode were also recorded for comparison (Fig. 4c). It is further proved that N-Ov-ZCO@CC have better electrochemical performance and higher energy storage efficiency than ZCO@CC. Moreover, the position shift in cathodic/anodic peaks with increased scan rates can be ascribed to the internal resistance and charge transfer limitations in the N-Ov-ZCO@CC electrode [49]. The improvement in electrochemical performance of N-Ov-ZCO@CC is mainly due to its high specific surface area with mesoporous structure and abundant chemical valence states, which provide large specific capacitance. The response of current density increases with scan rates, signifying the reduced resistance of electrode material and fast redox reactions at the electrode/electrolyte junction with good rate capability [50].

To better understand the ionic and electronic properties of materials in aqueous electrolyte, EIS was evaluated (Fig. 4i). The EIS spectra are composed of a semicircle in the high-frequency section and a linear component in the low-frequency section. In the high-frequency range, the *x*-intercept coincides with the R_s value, and the semicircle diameter coincides with the value of R_{ct}. The slope of the low-frequency range is larger, indicating that the diffusion resistance is smaller, enhancing the intercalation effect and improving the power density. The N-Ov-ZCO@CC electrode directs the lowest values of R_s = 1.94 Ω and R_{ct} = 0.38 Ω, better than ZCO@CC (R_s = 2.29 Ω and R_{ct} = 0. 46 Ω). N-Ov-ZCO@CC owns little resistance, which signifies its excellent electrochemical performance. The EIS results also signify the enhanced electrical conductivity and better electrochemical activity of N-Ov-ZCO@CC, attributed to the binder-free electrode structure and fast ionic diffusion.

Fig. 5a presents the comparative GCD curves at the current density of 1 A/g between 0.0–0.5 V. Each electrode shows a quasi-triangular shape of the GCD curves with a low voltage drop, revealing the reversible redox reactions and good conductivity [39]. Besides, the N-Ov-ZCO@CC electrode shows the longest discharge time and significantly improved specific capacitance, consistent with the CV analysis. Based on the discharge time in the GCD plots of the ZCO@CC and N-Ov-ZCO@CC at different current densities from 1 to 20 A/g (Fig. 5b-c), the calculated specific capacitances are summarized in Fig. 5d. It is worth mentioning that the pristine CC electrode has a very little discharge time at different current densities from 1 to 10 A/g (Fig. S4). The specific capacitance of the pristine CC electrode calculated by the discharge time is also very small compared with the N-Ov-ZCO@CC and ZCO@CC electrodes [51] (Fig. S5). The N-Ov-ZCO@CC exhibits the largest specific capacitance

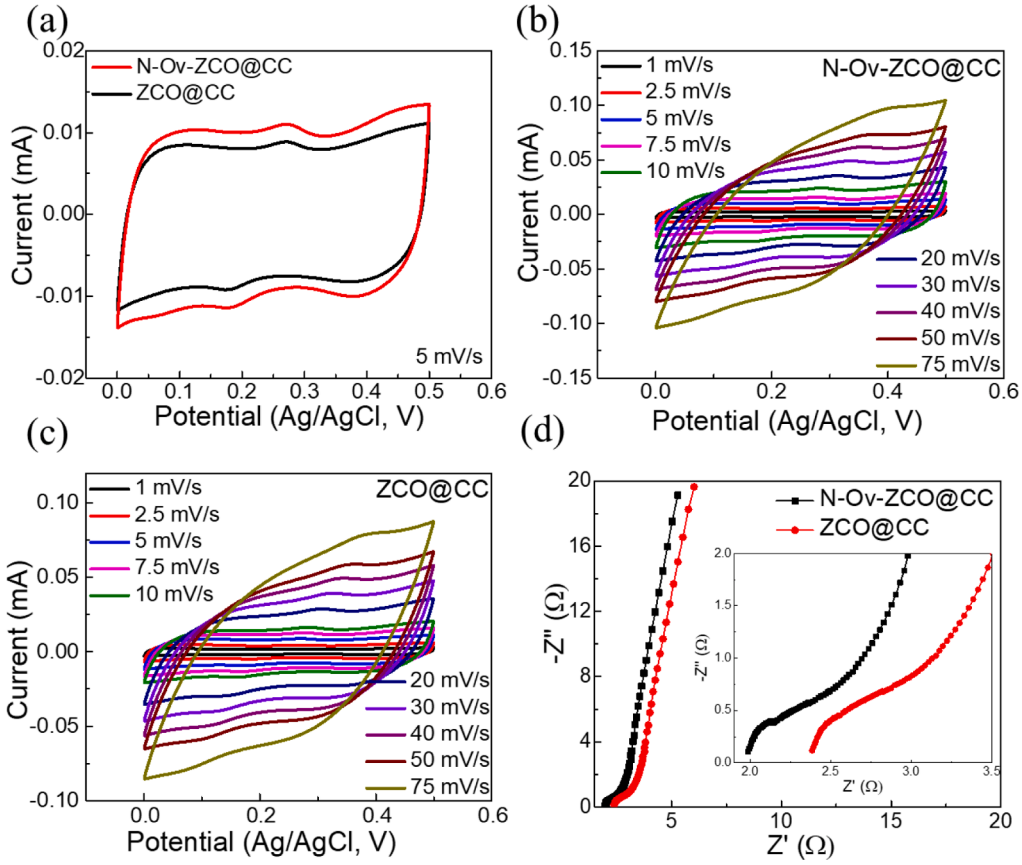

Fig. 4. (a) Comparative CV curves of N-Ov-ZCO@CC and ZCO@CC in potentials window of 0.0–0.5 V at 5 mV/s. CV curves at various scan rates for (b) N-Ov-ZCO@CC, (c) ZCO@CC electrode. (d) EIS spectrum of N-Ov-ZCO@CC and ZCO@CC.

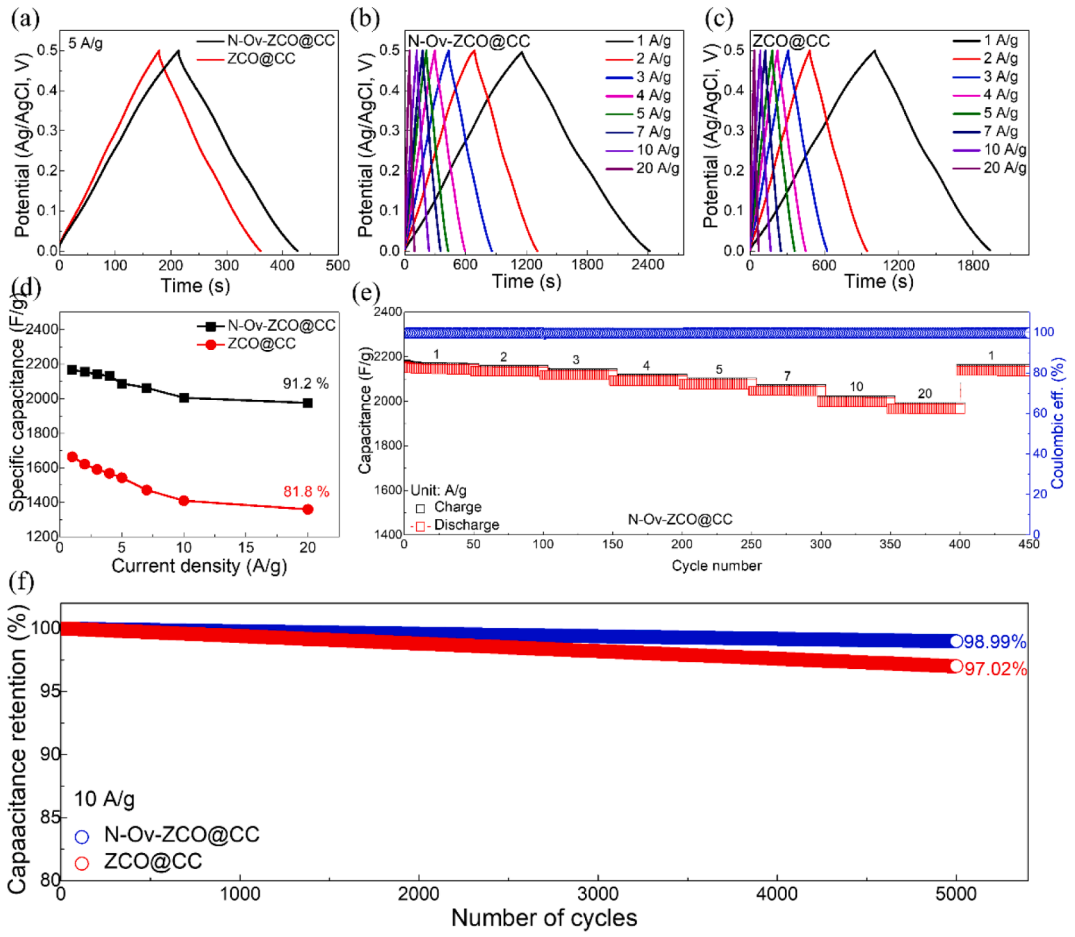

Fig. 5. (a) Comparative GCD curves of N-Ov-ZCO@CC and ZCO@CC in potentials window of 0.0–0.5 V at 5 A/g. GCD curves at various current densities range for (b) N-Ov-ZCO@CC, (c) ZCO@CC electrode. (d) Specific capacitance as a function of current density. (e) Rate capability and Coulombic efficiency versus the number of cycles up to 450 cycles. (g) Capacitance retention with respect to the number of cycles up to 5000 cycles for N-Ov-ZCO@CC and ZCO@CC.

under the same test conditions. The N-Ov-ZCO@CC yields an ultra-high capacitance of 2166.4 F/g at 1 A/g, remarkably larger than that of the ZCO@CC (1663.9 F/g at 1 A/g). About 91.2% of the initial capacitance can be kept with a twenty-fold increase in the current density, greatly exceeding that of the ZCO@CC (81.8%), suggesting the good rate performance of the N-Ov-ZCO@CC.

The rate performance of the N-Ov-ZCO@CC is shown in Fig. 5e. Specific discharge capacitances are 2180.4, 2107.9, 2076.8, 2066.6, 2031.6, 1981.8, 1951.8, and 1891.4 F/g at 1, 2, 3, 4, 5, 7, 10, and 20 A/g, respectively. Moreover, when the current density is reduced back to 1 A/g, a high discharge capacitance of 2121.4 F/g could be recovered with a recovery ratio of 97.3%, showing good electrochemical reversibility and fast reaction kinetics. The cycling stability tests for the sample were performed at a high current density of 10 A/g by running 5000 GCD cycles. The N-Ov-ZCO@CC exhibits astonishing cycling stability with capacitance retention of 98.99% after 5000 cycles, as compared with ZCO@CC (97.02%), and the results are summarized in Fig. 5f.

Zn-ion supercapacitor device was fabricated using N-Ov-ZCO@CC as the cathode and the Zn foil as the anode in a 6 M KOH + 0.2 M Zn-acetate aqueous electrolyte (Fig. 6a), denoted as N-Ov-ZCO@CC//Zn-ZHSC. Fig. 6b displays the CV curves of the N-Ov-ZCO@CC, Zn foil, and N-Ov-ZCO@CC//Zn-ZHSC at the scan rate of 10 mV/s within the potential ranging from 0.0 V to 0.5 V, −1.5 V to −0.5 V, and 1.2 V to 2.0 V, respectively. As shown in Fig. 6c, the CV curves for the ZHSC at various scan rates from 1 to 30 mV/s exhibit a typical pseudo-capacitive feature, primarily from the Faradic redox reactions on the N-Ov-ZCO@CC positive electrode. The similar shapes of the CV curves, even at the higher scan rates, infers good reversibility and fast ion/electron transport behaviors within the device. At the same potential window of 1.2–2.0 V, the GCD curves of N-Ov-ZCO@CC//Zn-ZHSC were recorded at various current densities (1–10 A/g), and the results are summarized in Fig. 6d. The highly symmetric GCD curves ensure excellent Coulombic efficiency and pseudocapacitive behavior [52]. Besides, the corresponding specific capacitances, calculated from the GCD curves as the function of current densities, as shown in Fig. 6e, where the impressive high capacitance of 280 F/g at the current density of 1 A/g is achieved. The ZHSC device can also maintain the comparable capacitance of 171.5 F/g even at a high current density of 10 A/g, reflecting the outstanding rate performance (61.3% capacitance retention).

It is impressive that the maximum specific energy densities of 155.68 Wh/kg at the power densities of 1000.8 W/kg are achieved and maintained to 95.35 Wh/kg at a high power density of 10,008 W/kg, exceeding the results of many previously reported ASC devices based on other bimetallic oxides, as results in Fig. 6f and Table 1. For example, BCN//Zn (119.7 Wh/kg at 890 W/kg) [53], $Cu_{0.82}Co_{0.18}HCF$//-$WO_3{\cdot}nH_2O$ (22 Wh/kg at 2600 W/kg) [54], OV-$ZnCo_2O_4$@NF//AC@NF (34.6 Wh/kg at 160 W/kg) [20], Mxene/rGO//Zn (34.9 Wh/kg at 279.9 W/kg) [55], N-$Ti_2C_3T_x$-MXene//Zn (16.7 Wh/kg at 6004.8 W/kg) [56], $ZnCo_2O_4$@$Ni_xCo_{2x}(OH)_{6x}$//AC (26.2 Wh/kg at 512 W/kg) [57], $ZnCo_2O_4$@$MnCo_2O_4$//AC (19.5 Wh/kg at 750 W/kg) [58], $ZnCo_2O_4$ NPs//MOF-NPC (18.0 Wh/kg at 2500 W/kg) [59]. The energy and power densities based on the whole mass of the N-Ov-ZCO@CC//Zn-ZHSC device were also calculated, as shown in Fig. S6. The N-Ov-ZCO@CC//Zn-ZHSC device exhibited an energy density of 1.55

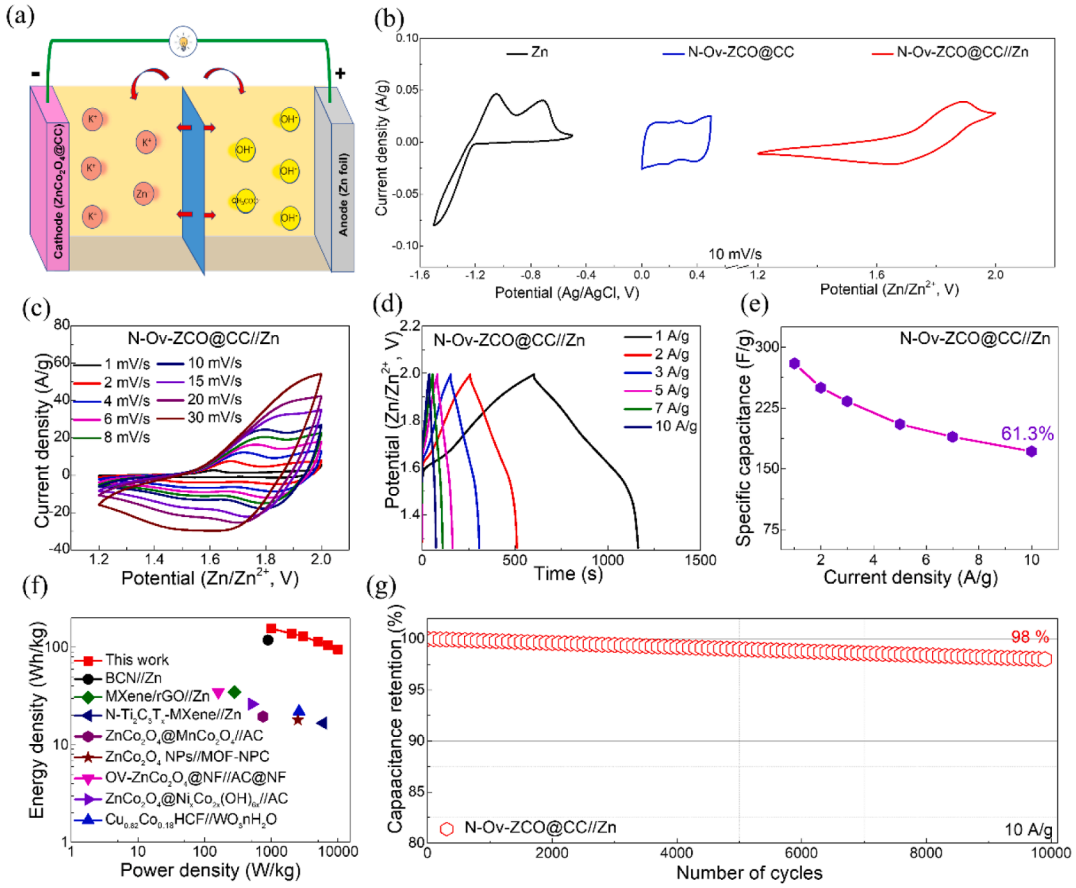

Fig. 6. (a) Schematically illustration of the fabricated ZHSC device. (b) CV curves of individual positive (N-Ov-ZCO@CC), negative (Zn foil), and N-Ov-ZCO@CC//Zn-ZHSC in the aqueous electrolyte at san rate of 10 mV/s in respective potential windows. (c) CV curves in the optimized window of 1.2–2.0 V at various scan rates. (d) GCD curves at various current densities in a potentials window of 1.2–2.0 V. (e) Specific capacitance as a function of current density. (f) A Ragone plot of the N-Ov-ZCO@CC//Zn-ZHSC based on the active mass on both electrodes along with a comparison with recently reported work. (h) Cycling performance test for as-fabricated N-Ov-ZCO@CC//Zn-ZHSC.

Table 1
Comparison of performance of Zn-ion hybrid supercapacitor based on asymmetric state with previous work.

No.	Cathode materials	Anode materials	electrolyte	E (Wh/kg)	P (W/kg)	Ref.
1	N-Ov-ZCO@CC	Zn foil	6 M KOH+0.2 M Zn(AC)	155.68	1000.8	This work
2	BCN	Zn foil	$ZnSO_4$/gelatin	119.7	890	[53]
3	$Cu_{0.82}Co_{0.18}HCF$	$WO_3{\cdot}nH_2O$	0.5 M H_2SO_4	22	2600	[54]
4	OV-$ZnCo_2O_4$@NF	AC@NF	6 M KOH	34.6	160	[20]
5	Mxene/rGO	Zn foil	2 M $ZnSO_4$	34.9	279.9	[55]
6	N-$Ti_2C_3T_x$–MXene	Zn foil	1 M $ZnSO_4$	16.7	6004.8	[56]
7	$ZnCo_2O_4$@$Ni_xCo_{2x}(OH)_{6x}$	AC	2 M KOH	26.2	512	[57]
8	$ZnCo_2O_4$@$MnCo_2O_4$	AC	6 M KOH	19.5	750	[58]
9	$ZnCo_2O_4$ NPs	MOF-NPC	6 M KOH	18.0	2500	[60]

Wh/kg at 20 W/kg and possessed 0.5 Wh/kg at a high power density of 200 W/kg. Furthermore, the cycling stability of the N-Ov-ZCO@CC//Zn-ZHSC was tested up to 10,000 cycles and showed good stability (98%) with high Coulombic efficiency (Fig. 6g).

4. Conclusion

In summary, we have successfully designed the novel N-Ov-ZCO@CC architectures on the CC substrate through the simple hydrothermal method and CVD strategy for high-performance ZHSC. Owing to the synergistic N-doping, oxygen vacancy, and surface micro and meso-porous characteristics, the N-Ov-ZCO@CC exhibits an ultra-high specific capacitance of 2166.4 F/g at 1 A/g, good rate capability, and remarkable cycling performance with capacitance retention of 98.99% after 5000 cycles. Furthermore, the Zinc-ion supercapacitors N-Ov-ZCO@CC//Zn-ZHSC can work at the extended potential window of 1.2–2.0 V and exhibit a high capacitance of 280 F/g at a current density of 1 A/g. And the N-Ov-ZCO@CC//Zn-ZHSC also has high energy and power densities (95.35 Wh/kg at 10,008 W/kg). Moreover, the device provides excellent stability with initial capacitance retention of 98% after 10,000 cycles. Consequently, N-Ov-ZCO@CC has excellent electrochemical properties, providing a new idea for developing new electrode materials for supercapacitors.

CRediT authorship contribution statement

Xiaofeng Zhang: Conceptualization, Methodology, Software. **Muhammad Sufyan Javed:** Conceptualization, Methodology,

Software, Supervision, Writing – review & editing. **Syed Shoaib Ahmad Shah:** Data curation, Writing – original draft. **Fahim Ahmed:** Data curation, Writing – original draft, Writing – review & editing. **Iftikhar Hussain:** Writing – review & editing. **Fatimah M. Alzahrani:** Software, Validation, Writing – review & editing. **Norah S. Alsaiari:** Software, Validation, Writing – review & editing. **Sayed M. Eldin:** Writing – review & editing, Writing – review & editing. **Mohd Zahid Ansari:** Data curation, Writing – original draft, Visualization, Investigation, Supervision, Writing – review & editing. **Weihua Han:** Supervision, Project administration, Validation, Visualization, Writing – review & editing.

Declaration of Competing Interest

The authors declare that they have no known competing financial interests or personal relationships that could have appeared to influence the work reported in this paper.

Data availability

Data will be made available on request.

Acknowledgments

This work was financially supported by the Research Fund for International Scientists (52250410342), a Scientific Research start-up grant for Youth Researchers at Lanzhou University, the National Natural Science Foundation of China (51972153), the Fundamental Research Funds for the Central Universities (lzujbky-2021-sp64) and Supercomputing Center of Lanzhou University. This research was funded by Princess Nourah bint Abdulrahman University Researchers Supporting Project number (PNURSP2023R42), Princess Nourah bint Abdulrahman University, Riyadh, Saudi Arabia

Supplementary materials

Supplementary material associated with this article can be found, in the online version, at doi:10.1016/j.electacta.2023.142654.

References

[1] M. Fu, W. Chen, Y. Lei, H. Yu, Y. Lin, M. Terrones, Biomimetic construction of ferrite quantum dot/graphene heterostructure for enhancing ion/charge transfer in supercapacitors, Adv. Mater. (2023), 2300940.
[2] C. Wan, Y. Jiao, D. Liang, Y. Wu, J. Li, A geologic architecture system-inspired micro-/nano-heterostructure design for high-performance energy storage, Adv. Energy Mater. 8 (33) (2018), 1802388.
[3] R. Ren, F. Lai, X. Lang, L. Li, C. Yao, K. Cai, Efficient sulfur host based on Sn doping to construct Fe2O3 nanospheres with high active interface structure for lithium-sulfur batteries, Appl. Surf. Sci. 613 (2023), 156003.
[4] C. Han, H. Wang, Z. Wang, X. Ou, Y. Tang, Solvation structure modulation of high-voltage electrolyte for high-performance K-based dual-graphite battery, Adv. Mater. (n/a) (2023), 2300917 n/a.
[5] L. Li, S. Jia, Z. Cheng, C. Zhang, Improved strategies for separators in zinc-ion batteries, ChemSusChem (2023), e202202330.
[6] S. Lu, Z. Yin, S. Liao, B. Yang, S. Liu, M. Liu, L. Yin, W. Zheng, An asymmetric encoder–decoder model for Zn-ion battery lifetime prediction, Energy Rep. 8 (2022) 33–50.
[7] H. Yu, Y. Chen, W. Wei, X. Ji, L. Chen, A functional organic zinc-chelate formation with nanoscaled granular structure enabling long-term and dendrite-free Zn anodes, ACS Nano 16 (6) (2022) 9736–9747.
[8] Y. Liu, Q. Li, K. Ma, G. Yang, C. Wang, Graphene oxide wrapped CuV2O6 nanobelts as high-capacity and long-life cathode materials of aqueous zinc-ion batteries, ACS Nano 13 (10) (2019) 12081–12089.
[9] V. Soundharrajan, B. Sambandam, S. Kim, M.H. Alfaruqi, D.Y. Putro, J. Jo, S. Kim, V. Mathew, Y.-K. Sun, J. Kim, Na2V6O16· 3H2O barnesite nanorod: an open door to display a stable and high energy for aqueous rechargeable Zn-ion batteries as cathodes, Nano Lett. 18 (4) (2018) 2402–2410.
[10] F. Wan, Y. Zhang, L. Zhang, D. Liu, C. Wang, L. Song, Z. Niu, J. Chen, Reversible oxygen redox chemistry in aqueous zinc-ion batteries, Angew. Chem. Int. Ed. 58 (21) (2019) 7062–7067.
[11] S.-M. Lee, Y.-J. Park, J.-H. Kim, K. Lee, Effects of annealing on electrochemical performance in graphene/V2O5 supercapacitor, Appl. Surf. Sci. 512 (2020), 145626.
[12] M. Chamoun, W. Brant, C. Tai, G. Karlsson, D. Noréus, Rechargeability of aqueous sulfate Zn/MnO2 batteries enhanced by accessible Mn2+ ions, Energy Storage Mater. 15 (2018) 351–360.
[13] S. Zhao, B. Han, D. Zhang, Q. Huang, L. Xiao, L. Chen, D.G. Ivey, Y. Deng, W. Wei, Unravelling the reaction chemistry and degradation mechanism in aqueous Zn/MnO 2 rechargeable batteries, J. Mater. Chem. A 6 (14) (2018) 5733–5739.
[14] W. Guo, C. Yu, S. Li, Z. Wang, J. Yu, H. Huang, J. Qiu, Strategies and insights towards the intrinsic capacitive properties of MnO2 for supercapacitors: challenges and perspectives, Nano Energy 57 (2019) 459–472.
[15] Z. He, Y. Wang, Y. Li, J. Ma, Y. Song, X. Wang, F. Wang, Superior pseudocapacitive performance and mechanism of self-assembled MnO2/MXene films as positive electrodes for flexible supercapacitors, J. Alloys Compd. 899 (2022), 163241.
[16] Z. Guo, Y. Li, Z. Lu, Y. Chao, W. Liu, High-performance MnO2@ MXene/carbon nanotube fiber electrodes with internal and external construction for supercapacitors, J. Mater. Sci. 57 (5) (2022) 3613–3628.
[17] Y. Zeng, Z. Lai, Y. Han, H. Zhang, S. Xie, X. Lu, Oxygen-vacancy and surface modulation of ultrathin nickel cobaltite nanosheets as a high-energy cathode for advanced Zn-Ion batteries, Adv. Mater. 30 (33) (2018), 1802396.
[18] C. Xu, J. Tan, X. Zhang, Y. Huang, Petal-like CuCo2O4 spinel nanocatalyst with rich oxygen vacancies for efficient PMS activation to rapidly degrade pefloxacin, Sep. Purif. Technol. 291 (2022), 120933.
[19] D. He, M. Wang, X. Wang, S. Feng, J. Chen, P. Jiang, Construction of ZnCo2O4 nanowire arrays 3D binder-free electrode with highly catalytic activity towards glucose oxidation, J. Solid State Chem. 284 (2020), 121214.
[20] K. Xiang, D. Wu, Y. Fan, W. You, D. Zhang, J.-L. Luo, X.-Z. Fu, Enhancing bifunctional electrodes of oxygen vacancy abundant ZnCo2O4 nanosheets for supercapacitor and oxygen evolution, Chem. Eng. J. 425 (2021), 130583.
[21] A. Konarov, N. Voronina, J.H. Jo, Z. Bakenov, Y.-K. Sun, S.-T. Myung, Present and future perspective on electrode materials for rechargeable zinc-ion batteries, ACS Energy Lett. 3 (10) (2018) 2620–2640.
[22] H. Liu, M. Dai, D. Zhao, X. Wu, B. Wang, Realizing superior electrochemical performance of asymmetric capacitors through tailoring electrode architectures, ACS Appl. Energy Mater. 3 (7) (2020) 7004–7010.
[23] Q. Ma, F. Cui, J. Zhang, T. Cui, Built-in electric field boosted ionic transport kinetics in the heterostructured ZnCo2O4/ZnO nanobelts for high-performance supercapacitor, J. Colloid Interface Sci. (2022).
[24] X. Chen, N. Xin, Y. Li, C. Sun, L. Li, Y. Ying, W. Shi, Y. Liu, Novel 2D/2D NiCo2O4/ZnCo2O4@ rGO/CNTs self-supporting composite electrode with high hydroxyl ion adsorption capacity for asymmetric supercapacitor, J. Mater. Sci. Technol. 127 (2022) 236–244.
[25] L. Yuan, Y. Liu, N. Xin, R. He, Hierarchical structure ZnCo2O4/ZnCo2O4/CoO@ rGO/GO as cathode material to construct high energy density supercapacitor, J. Energy Storage 52 (2022), 104727.
[26] Z. Wu, X. Yang, H. Gao, H. Shen, H. Wu, X. Xia, X. Wu, W. Lei, J. Yang, Q. Hao, Controllable synthesis of ZnCo2O4@ NiCo2O4 heterostructures on Ni foam for hybrid supercapacitors with superior performance, J. Alloys Compd. 891 (2022), 162053.
[27] I.K. Moon, S. Yoon, B. Ki, K. Choi, J. Oh, Remarkable enhancement of electrochemical performance by the oxygen vacancy and nitrogen doping in ZnCo2O4 nanowire arrays, ACS Appl. Energy Mater. 1 (9) (2018) 4804–4813.
[28] S. Liu, Y. Yin, D. Ni, K. San Hui, K.N. Hui, S. Lee, C.-Y. Ouyang, S.C. Jun, Phosphorous-containing oxygen-deficient cobalt molybdate as an advanced electrode material for supercapacitors, Energy Storage Mater. 19 (2019) 186–196.
[29] K. Choi, I.K. Moon, J. Oh, An efficient amplification strategy for N-doped NiCo 2 O 4 with oxygen vacancies and partial Ni/Co-nitrides as a dual-function electrode for both supercapatteries and hydrogen electrocatalysis, J. Mater. Chem. A 7 (4) (2019) 1468–1478.
[30] Y. Niu, D. Wang, Y. Ma, L. Zhi, Cascading V2O3/N-doped carbon hybrid nanosheets as high-performance cathode materials for aqueous zinc-ion batteries, Chin. Chem. Lett. 33 (3) (2022) 1430–1434.
[31] Y. Zhang, L. Tao, C. Xie, D. Wang, Y. Zou, R. Chen, Y. Wang, C. Jia, S. Wang, Defect engineering on electrode materials for rechargeable batteries, Adv. Mater. 32 (7) (2020), 1905923.
[32] G. Li, S. Huang, K. Li, N. Zhu, B. Zhao, Q. Zhong, Z. Zhang, D. Ge, D. Wang, Near-infrared responsive Z-scheme heterojunction with strong stability and ultra-high quantum efficiency constructed by lanthanide-doped glass, Appl. Catal. B Environ. 311 (2022), 121363.
[33] J. Lin, Z. Zhong, H. Wang, X. Zheng, Y. Wang, J. Qi, J. Cao, W. Fei, Y. Huang, J. Feng, Rational constructing free-standing Se doped nickel-cobalt sulfides nanotubes as battery-type electrode for high-performance supercapattery, J. Power Sources 407 (2018) 6–13.
[34] H. Liang, H. Jia, T. Lin, Z. Wang, C. Li, S. Chen, J. Qi, J. Cao, W. Fei, J. Feng, Oxygen-vacancy-rich nickel-cobalt layered double hydroxide electrode for high-performance supercapacitors, J. Colloid Interface Sci. 554 (2019) 59–65.
[35] Z. Liu, Y. Qiu, L. Cui, R. Zheng, W. Yang, C.J. Barrow, J.M. Razal, J. Liu, Water-based asymmetric supercapacitors with 2.5 V wide potential and high energy density based on Na0. 6CoO2 nanoarray formed via electrochemical oxidation, Carbon N Y 189 (2022) 81–92.
[36] Z. Pang, B. Wang, X. Yan, C. Wang, S. Yin, H. Li, J. Xia, CdBiO2Br nanosheets in situ strong coupling to carbonized polymer dots and improved photocatalytic activity for organic pollutants degradation, Chin. Chem. Lett. 33 (12) (2022) 5189–5195.

[37] M.S. Javed, I. Hussain, S. Batool, S.H. Siyal, T. Najam, S.S.A. Shah, M. Imran, M. A. Assiri, S. Hussain, Energy storage properties of hydrothermally processed ultrathin 2D binder-free ZnCo2O4 nanosheets, Nanotechnology 32 (38) (2021), 385402.
[38] B. Chakraborty, A. Indra, P. Menezes, M. Drieß, P. Menezes, Improved chemical water oxidation with Zn in the tetrahedral site of spinel-type ZnCo2O4 nanostructure, Mater. Today Chem. 15 (2020), 100226.
[39] S. Wei, C. Wan, L. Zhang, X. Liu, W. Tian, J. Su, W. Cheng, Y. Wu, N-doped and oxygen vacancy-rich NiCo2O4 nanograss for supercapacitor electrode, Chem. Eng. J. 429 (2022), 132242.
[40] C.-F. Li, J.-W. Zhao, L.-J. Xie, J.-Q. Wu, G.-R. Li, Fe doping and oxygen vacancy modulated Fe-Ni5P4/NiFeOH nanosheets as bifunctional electrocatalysts for efficient overall water splitting, Appl. Catal. B Environ. 291 (2021), 119987.
[41] J.J. Carey, M. Legesse, M. Nolan, Low valence cation doping of bulk Cr2O3: charge compensation and oxygen vacancy formation, J. Phys. Chem. C 120 (34) (2016) 19160–19174.
[42] N. Li, G. Qu, X. Zhang, S. Zhao, C. Wang, G. Zhao, P. Hou, X. Xu, Amorphous Ni-Co-S nanocages assembled with nanosheet arrays as cathode for high-performance zinc ion battery, Chin. Chem. Lett. 33 (6) (2022) 3272–3276.
[43] G.P. Sharma, P.K. Gupta, S.K. Sharma, R.G.S. Pala, S. Sivakumar, Chalcogenide dopant-induced lattice expansion in cobalt vanadium oxide nanosheets for enhanced supercapacitor performance, ACS Appl. Energy Mater. 4 (5) (2021) 4758–4771.
[44] Z. Zhu, P. Liu, Y. Liu, X. Gu, Z. Su, Z. Su, C.J.C.C.L. Lai, Defect-rich and highly porous carbon nanosheets derived from Ti3AlC2 MAX with good lithium storage properties, Chin. Chem. Lett. 34 (2) (2023), 107228.
[45] Y. Zhang, J. Ding, W. Xu, M. Wang, R. Shao, Y. Sun, B. Lin, Mesoporous LaFeO3 perovskite derived from MOF gel for all-solid-state symmetric supercapacitors, Chem. Eng. J. 386 (2020), 124030.
[46] J. Zhang, L.-B. Kong, J.-J. Cai, H. Li, Y.-C. Luo, L. Kang, Hierarchically porous nickel hydroxide/mesoporous carbon composite materials for electrochemical capacitors, Microporous Mesoporous Mater. 132 (1–2) (2010) 154–162.
[47] G. Gou, F. Huang, M. Jiang, J. Li, Z. Zhou, Hierarchical porous carbon electrode materials for supercapacitor developed from wheat straw cellulosic foam, Renew Energy 149 (2020) 208–216.
[48] N.R. Chodankar, S. Selvaraj, S.H. Ji, Y. Kwon, D.H. Kim, Interface-engineered nickel cobaltite nanowires through NiO atomic layer deposition and nitrogen plasma for high-energy, long-cycle-life foldable all-solid-state supercapacitors, Small 15 (3) (2019), 1803716.
[49] B. Huang, H. Wang, S. Liang, H. Qin, Y. Li, Z. Luo, C. Zhao, L. Xie, L. Chen, Two-dimensional porous cobalt–nickel tungstate thin sheets for high performance supercapattery, Energy Storage Mater. 32 (2020) 105–114.
[50] Z. Huang, P. Luo, H. Zheng, Z. Lyu, X. Ma, Novel one-dimensional V3S4@ NC nanofibers for sodium-ion batteries, J. Phys. Chem. Solids 172 (2023), 111081.
[51] A.C. Castro Neto, F. Guinea, N.M.R. Peres, K.S. Novoselov, A.K. Geim, The electronic properties of graphene, Rev. Mod. Phys. 81 (1) (2009) 109.
[52] H. Fan, X. Hu, S. Zhang, Z. Xu, G. Gao, Y. Zheng, G. Hu, Q. Chen, T.S. AlGarni, R. Luque, Flower-like carbon cathode prepared via in situ assembly for Zn-ion hybrid supercapacitors, Carbon N Y 180 (2021) 254–264.
[53] T. Xu, Z. Li, D. Wang, M. Zhang, L. Ai, Z. Chen, J. Zhang, X. Zhang, L. Shen, A fast proton-induced pseudocapacitive supercapacitor with high energy and power density, Adv. Funct. Mater. 32 (5) (2022), 2107720.
[54] Q. Wang, S. Wang, X. Guo, L. Ruan, N. Wei, Y. Ma, J. Li, M. Wang, L. Wanqing, W. Zeng, Mxene-reduced graphene oxide aerogel for aqueous zinc-ion hybrid supercapacitor with ultralong cycle life, Adv. Electron. Mater. 5 (12) (2019), 1900537.
[55] A. Mateen, M.Z. Ansari, Q. Abbas, A. Muneeb, A. Hussain, E.T. Eldin, F. M. Alzahrani, N.S. Alsaiari, S. Ali, M.S. Javed, In Situ nitrogen functionalization of 2D-Ti3C2T x-MXenes for high-performance Zn-Ion supercapacitor, Molecules 27 (21) (2022) 7446.
[56] W. Fu, Y. Wang, W. Han, Z. Zhang, H. Zha, E. Xie, Construction of hierarchical ZnCo 2 O 4@ Ni x Co 2x (OH) 6x core/shell nanowire arrays for high-performance supercapacitors, J. Mater. Chem. A 4 (1) (2016) 173–182.
[57] L. Wang, Y. Guan, X. Zhao, J. Mu, H. Che, H. Li, Z. Guo, ZnCo2O4@ MnCo2O4 heterojunction structured nanosheets for high-performance supercapacitor, J. Mater. Sci. Mater. Electron. 29 (7) (2018) 5782–5790.
[58] D. He, Y. Gao, Y. Yao, L. Wu, J. Zhang, Z.-H. Huang, M.-X. Wang, Asymmetric supercapacitors based on hierarchically nanoporous carbon and ZnCo2O4 from a single biometallic metal-organic frameworks (Zn/Co-MOF), Front. Chem. (2020) 719.
[59] M.S. Javed, H. Lei, H.U. Shah, S. Asim, R. Raza, W. Mai, Achieving high rate and high energy density in an all-solid-state flexible asymmetric pseudocapacitor through the synergistic design of binder-free 3D ZnCo2O4 nano polyhedra and 2D layered Ti3C2Tx-MXenes, J. Mater. Chem. A 7 (42) (2019) 24543–24556.
[60] D. He, Y. Gao, Y. Yao, L. Wu, J. Zhang, Z.H. Huang, M.X. Wang, Asymmetric supercapacitors based on hierarchically nanoporous carbon and ZnCo2O4 from a single biometallic metal-organic frameworks (Zn/Co-MOF), Front. Chem. 8 (2020) 719.